ACS NANO

www.acsnano.org

ARTICLE

Harnessing 2D Ruddlesden–Popper Perovskite with Polar Organic Cation for Ultrasensitive Multibit Nonvolatile Transistor-Type Photomemristors

Po-Ting Lai, Cheng-Yueh Chen, Hao-Cheng Lin, Bo-Yuan Chuang, Kai-Hua Kuo, Christopher R. Greve, Tsung-Kai Su, Guang-Hsun Tan, Chia-Feng Li, Sheng-Wen Huang, Kai-Yuan Hsiao, Eva M. Herzig, Ming-Yen Lu, Yu-Ching Huang, Ken-Tsung Wong,* and Hao-Wu Lin*

Cite This: *ACS Nano* 2023, 17, 25552–25564

Read Online

ACCESS | Metrics & More | Article Recommendations | Supporting Information

ABSTRACT: Photomemristors have been regarded as one of the most promising candidates for next-generation hardware-based neuromorphic computing due to their potentials of fast data transmission and low power consumption. However, intriguingly, so far, photomemristors seldom display truly nonvolatile memory characteristics with high light sensitivity. Herein, we demonstrate ultrasensitive photomemristors utilizing two-dimensional (2D) Ruddlesden–Popper (RP) perovskites with a highly polar donor–acceptor-type push–pull organic cation, 4-(5-(2-aminoethyl)thiophen-2-yl)-benzonitrile$^+$ (EATPCN$^+$), as charge-trapping layers. High linearity and almost zero-decay retention are observed in $(EATPCN)_2PbI_4$ devices, which are very distinct from that of the traditional 2D RP perovskite devices consisting of nonpolar organic cations, such as phenethylamine$^+$ (PEA$^+$) and octylamine$^+$ (OA$^+$), and traditional 3D perovskite devices consisting of methylamine$^+$ (MA$^+$). The 2-fold advantages, including desirable spatial crystal arrangement and engineered energetic band alignment, clarify the mechanism of superior performance in $(EATPCN)_2PbI_4$ devices. The optimized $(EATPCN)_2PbI_4$ photomemristor also shows a memory window of 87.9 V and an on/off ratio of 10^6 with a retention time of at least 2.4×10^5 s and remains unchanged after $>10^5$ writing–reading–erasing–reading endurance cycles. Very low energy consumptions of 1.12 and 6 fJ for both light stimulation and the reading process of each status update are also demonstrated. The extremely low power consumption and high photoresponsivity were simultaneously achieved. The high photosensitivity surpasses that of a state-of-the-art commercial pulse energy meter by several orders of magnitude. With their outstanding linearity and retention, rabbit images have been rebuilt by $(EATPCN)_2PbI_4$ photomemristors, which truthfully render the image without fading over time. Finally, by utilizing the powerful ∼8 bits of nonvolatile potentiation and depression levels of $(EATPCN)_2PbI_4$ photomemristors, the accuracies of the recognition tasks of CIFAR-10 image classification and MNIST handwritten digit classification have reached 89% and 94.8%, respectively. This study represents the first report of utilizing a functional donor–acceptor type of organic cation in 2D RP perovskites for high-performance photomemristors with characteristics that are not found in current halide perovskites.

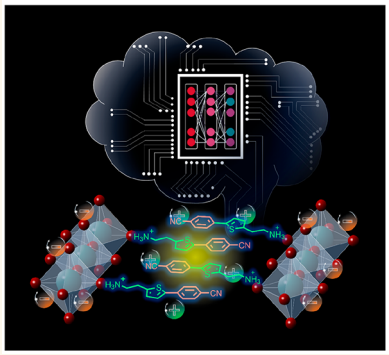

KEYWORDS: *Ruddlesden–Popper perovskite, photomemristors, push–pull organic cation, multibit nonvolatile memory, low energy consumption, high light sensitivity*

INTRODUCTION

Brain-inspired neuromorphic computing is a promising approach for energy-efficient and time-saving massive data computing, leveraging the principles of parallel computing.[1,2] One of the critical components for hardware-based neuromorphic computing is the memristor, particularly those capable of storing multibit or analog memory. Multibit memristors mimic the continuously variable potentiation and depression of synapses and neurons in the human brain.

Received: October 4, 2023
Revised: December 5, 2023
Accepted: December 8, 2023
Published: December 14, 2023

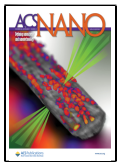

https://doi.org/10.1021/acsnano.3c09595
ACS Nano 2023, 17, 25552–25564

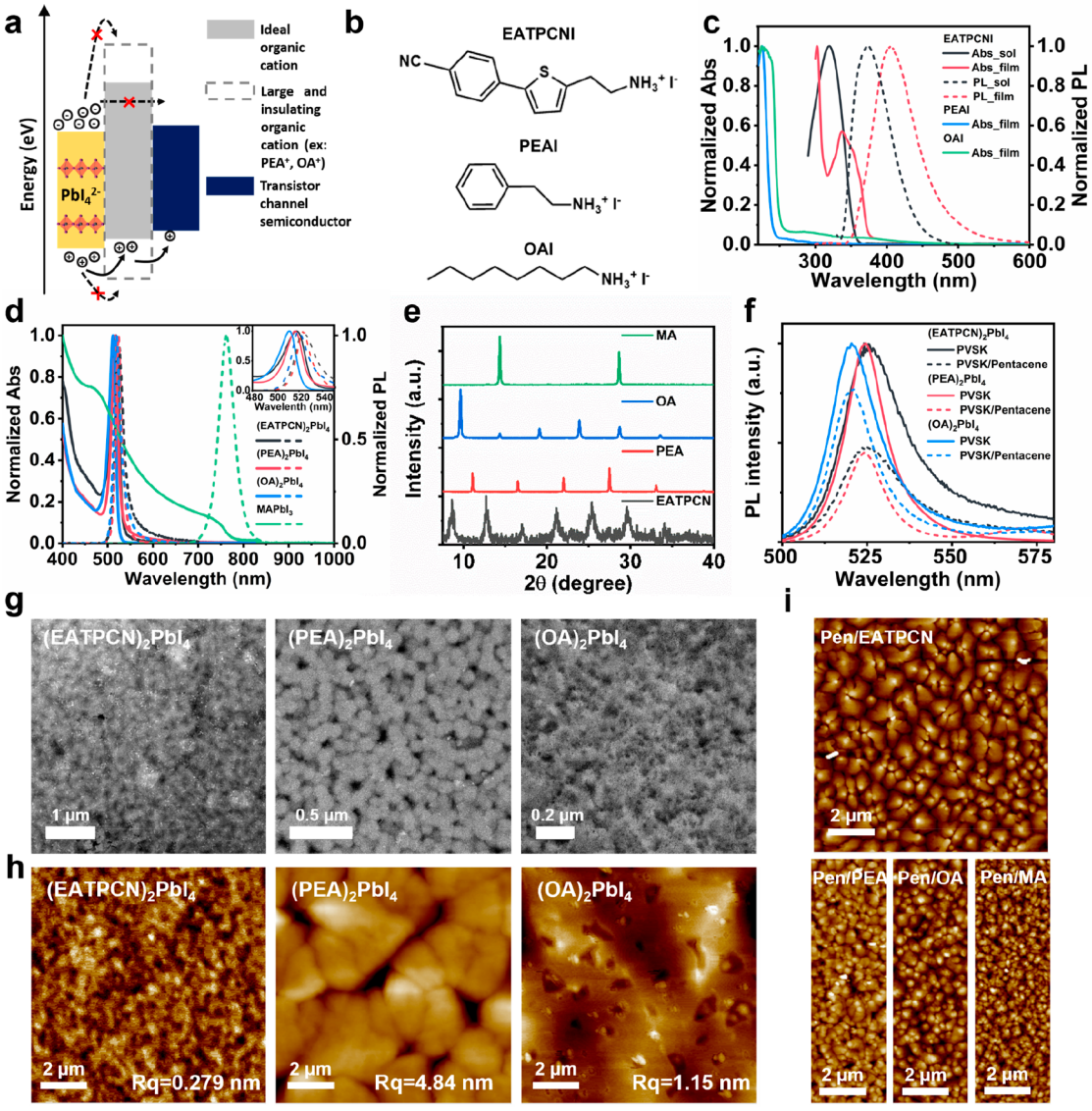

Figure 1. Ideal band alignment of floating-gate memristors and characterizations of perovskite films. (a) Illustration of suitable energy level alignment of suitable or common organic cation, PbI_4^{2-} and transistor channel semiconductor. (b) Molecular structure of EATPCNI, PEAI, and OAI. (c) Normalized absorption (solid lines) of EATPCNI (solution in black and film in red), PEAI (blue line), and OAI (green line). Normalized photoluminescence of EATPCNI in solution (black dashed line) and film (red dashed line) types. (d) Normalized absorption and PL spectra of $(EATPCN)_2PbI_4$ (black lines), $(PEA)_2PbI_4$ (red lines), $(OA)_2PbI_4$ (blue lines), and $MAPbI_3$ (green lines) neat films. (e) XRD patterns of $(EATPCN)_2PbI_4$, $(PEA)_2PbI_4$, $(OA)_2PbI_4$, and $MAPbI_3$ neat films. (f) PL intensities of neat 2D perovskite films and those quenched by pentacene. (g) STEM image of $(EATPCN)_2PbI_4$ film (left), $(PEA)_2PbI_4$ film (middle), and $(OA)_2PbI_4$ film (right). (h) AFM images of $(EATPCN)_2PbI_4$ film (left), $(PEA)_2PbI_4$ film (middle), and $(OA)_2PbI_4$ film (right). The extremely smooth morphology, R_q = 0.279 nm, is owned by $(EATPCN)_2PbI_4$ neat film. (i) The upper is the AFM image of pentacene grown on $(EATPCN)_2PbI_4$ film and the lower is the AFM image of pentacene grown on $(PEA)_2PbI_4$ film (left), $(OA)_2PbI_4$ film (middle), and $MAPbI_3$ film (right).

Memristors can be integrated into large-scale arrays to form artificial neural networks (ANNs). The use of hardware-based implementations of ANNs has the potential to outperform current software-based approaches.[3−5]

While the majority of memristor research has focused on electrically stimulated devices, researchers started to develop photonic memristors for photonic ANNs recently. Photonic ANNs offer potential advantages over their electronic counterparts, including extremely low power consumption, high speed, less-interfering parallel processing, and wavelength-dependent multiplexing.[6−8] Moreover, the integration of neuromorphic functions with photonic sensing enables applications such as direct pattern recognition, neuromorphic vision sensing, and collision detection.[6,9]

Photonic memristors, or photomemristors, can be divided into two types: resistor-like two-terminal devices[10,11] or transistor-like three-terminal devices.[12−14] Among these, the three-terminal photomemristors have garnered particular interest, especially those that utilize separate materials for the photoactive layer and the transistor channel layer. These devices offer the greatest decoupling of the stimuli and status reading electric pathways, displaying the potential for individually optimizing each functional layer.[15−17]

Halide perovskites are promising materials for optoelectronic applications such as solar cells, light-emitting diodes,

https://doi.org/10.1021/acsnano.3c09595
ACS Nano 2023, 17, 25552−25564

and photodetectors, owing to their outstanding properties, including long charge carrier lifetime, small exciton binding energy, and tunable bandgap.[18−21] Large light absorption coefficient, excellent photosensitivity, and low exciton binding energy make halide perovskites potential candidates as photosensitive layers of photomemristors.[22,23] Light-induced excitons in the perovskite layer dissociate into electrons and holes, allowing for trapping one type of charge carrier in the floating gate. Zhou and Han's groups utilized suspended $CsPbBr_3$ quantum dots (QDs) in a poly(methyl methacrylate) (PMMA) matrix as the photosensitive floating-gate layer and pentacene as the channel layer.[24] The $CsPbBr_3$ QDs were found to effectively trap electrons, demonstrating the potential of employing halide perovskites in photomemristors. Apart from 3D perovskites, 2D perovskites are also possible options for perovskite floating-gate photomemristors, because cations with a large bandgap for 2D perovskites may form a natural energy barrier for enhancing the carriers' trapping ability.[25] Despite the great potential of using halide perovskites as the photoactive layer in photonic memristors, so far, perovskite-based photomemristors still suffer from few memory states and high stimulus light intensity and are not truly nonvolatile, as they exhibit certain decay before stabilizing to a constant memory state.

To tackle these issues, in this paper, a donor−acceptor-type organic cation, 4-(5-(2-aminoethyl)thiophen-2-yl)-benzonitrile$^+$ (EATPCN$^+$), is designed to form $(EATPCN)_2PbI_4$, a 2D Ruddlesden−Popper perovskite (2D-RPP) with a highly polar organic cation in the perovskite crystals. The $(EATPCN)_2PbI_4$ layer was utilized as the ultrasensitive photosensitive floating-gate layer that was integrated with the pentacene-based field effective transistor. The resulting $(EATPCN)_2PbI_4$ photomemristors exhibit excellent performance, including truly nonvolatile 250-level memory with almost zero decay and high linearity, a very wide memory window of 87.9 V, an on/off ratio of 10^6, a long retention time of at least 2.4×10^5 s, and excellent endurance of $>10^5$ cycles, with femtojoule energy consumption in both the stimulation and state-reading processes. The superhigh sensitivity, coupled with its nonvolatile characteristics, positions these devices as standalone, single-device-based energy meters capable of detecting pulse energy at the femtojoule level, surpassing the performance of the current best commercial energy meters by several orders of magnitude. Moreover, benefitting from the outstanding linearity and retention ability, an extracted rabbit image has been rebuilt by a $(EATPCN)_2PbI_4$ photomemristor, which truthfully renders the image without fading over time. As a consequence of their highly linear nonvolatile multilevel memory states, the accuracies of the recognition tasks of the Canadian Institute for Advanced Research-10 (CIFAR-10) image classification and Modified National Institute of Standards and Technology (MNIST) handwritten digit classification have reached 89% and 94.8%, respectively. This work highlights an approach of designing a 2D-RPP for photomemristor applications.

RESULTS AND DISCUSSION

Fabrications and Characterizations of 2D Perovskite Films. 3D perovskites, such as $CsPbBr_3$ and $MAPbI_3$ ($MA^+ = CH_3NH_3^+$), exhibit high carrier mobility, which is highly desirable for photovoltaic or light emission applications. However, this high carrier mobility can largely hinder the carrier-trapping capability, resulting in volatile memory characteristics. In contrast, incorporating a large insulating organic cation to form 2D or quasi-2D perovskites can effectively trap one type of charge carrier in the floating gate. The large-bandgap nature of these organic cations also makes it difficult for the other type of charge carriers to escape from the floating gate, resulting in poor sensitivity. Hence, in 2D or quasi-2D perovskite photomemristors, high stimulation light intensity is still required, and the response time is usually slow.

We believe that the ideal organic cation for 2D RP perovskite should have a highest occupied molecular orbital (HOMO) energy level aligned with the conduction level of the central 2D lead halide layer: in this case, the PbI_4^{2-} layer. Such energy level alignments allow holes to easily escape from the 2D PbI_4^{2-} layer to the transistor channel layer, which in the current case is pentacene. The lowest unoccupied molecular orbital (LUMO), on the other hand, should be high-lying to facilitate good electron trapping, as illustrated in Figure 1a. A dedicated molecule, EATPCN$^+$, designed to meet these requirements, is shown in Figure 1b along with the traditional large-bandgap organic cations phenethylamine$^+$ (PEA$^+$) and octylamine$^+$ (OA$^+$), commonly used in 2D RP perovskites. EATPCN$^+$ is composed of an electron-rich thiophene and an electron-deficient benzonitrile group, endowing this molecule with a high dipole moment and desirable HOMO and LUMO levels. The detailed synthetic route of EATPCN$^+$ is shown in Scheme S1 in the Supporting Information. Figure 1c shows the absorption spectra of 2-(5-(4-cyanophenyl)thiophen-2-yl)-ethan-1-aminium iodide (EATPCNI), PEAI, and OAI. Obviously, PEAI and OAI show a larger bandgap than EATPCNI. The EATPCNI shows the photoluminescence (PL) peaking at 374 and 420 nm in solution and film, respectively. The distinct absorption spectra observed in the solution and solid states of EATPCNI may be attributed to the differences in molecular packing between these two phases. The significantly red-shifted emission spectrum of the EATPCNI film, compared to its toluene solution counterpart, further confirms the highly polar nature of EATPCNI, influenced by the solvation effect. The 2D perovskite was made up with a 2:1 molar ratio of organic halides and PbI_2, resulting in $(EATPCN)_2PbI_4$, $(PEA)_2PbI_4$, and $(OA)_2PbI_4$. A traditional 3D perovskite, $MAPbI_3$, was also prepared for comparison. Figure 1d depicts the absorption and PL spectra of these perovskites. Similar PL centered at 524, 523, and 520 nm in $(EATPCN)_2PbI_4$, $(PEA)_2PbI_4$, and $(OA)_2PbI_4$ indicates the effective formation of a similar 2D perovskite with PbI_4^{2-} quantum wells, while the PL peaking at 762 nm matches the reported $MAPbI_3$.[26,27] The X-ray diffraction information on perovskites is summarized in Figure 1e. All 2D perovskite samples display the signature (00l) crystalline structure (l = 2, 4, 6, ...) with various d-spacing due to the size effect of organic cations. Apparently, $(PEA)_2PbI_4$ and $(OA)_2PbI_4$ exhibit much sharper diffraction peaks as compared to those of $(EATPCN)_2PbI_4$, indicating larger crystals and more long-range order. We believe that the structural feature of EATPCN is responsible for the retardation of formation of large crystals. This speculation was confirmed later by grazing-incidence wide-angle X-ray scattering (GIWAXS) measurements. Furthermore, for the three-terminal transistor-type photomemristor, it is important to examine the photoinduced charge transfer between the trapping and channel layers. The PL intensities with and without the channel layer pentacene were measured, and the results are shown in Figure 1f. The PL intensity of $(EATPCN)_2PbI_4$ and $(PEA)_2PbI_4$ is 51.7% and

https://doi.org/10.1021/acsnano.3c09595
ACS Nano 2023, 17, 25552−25564

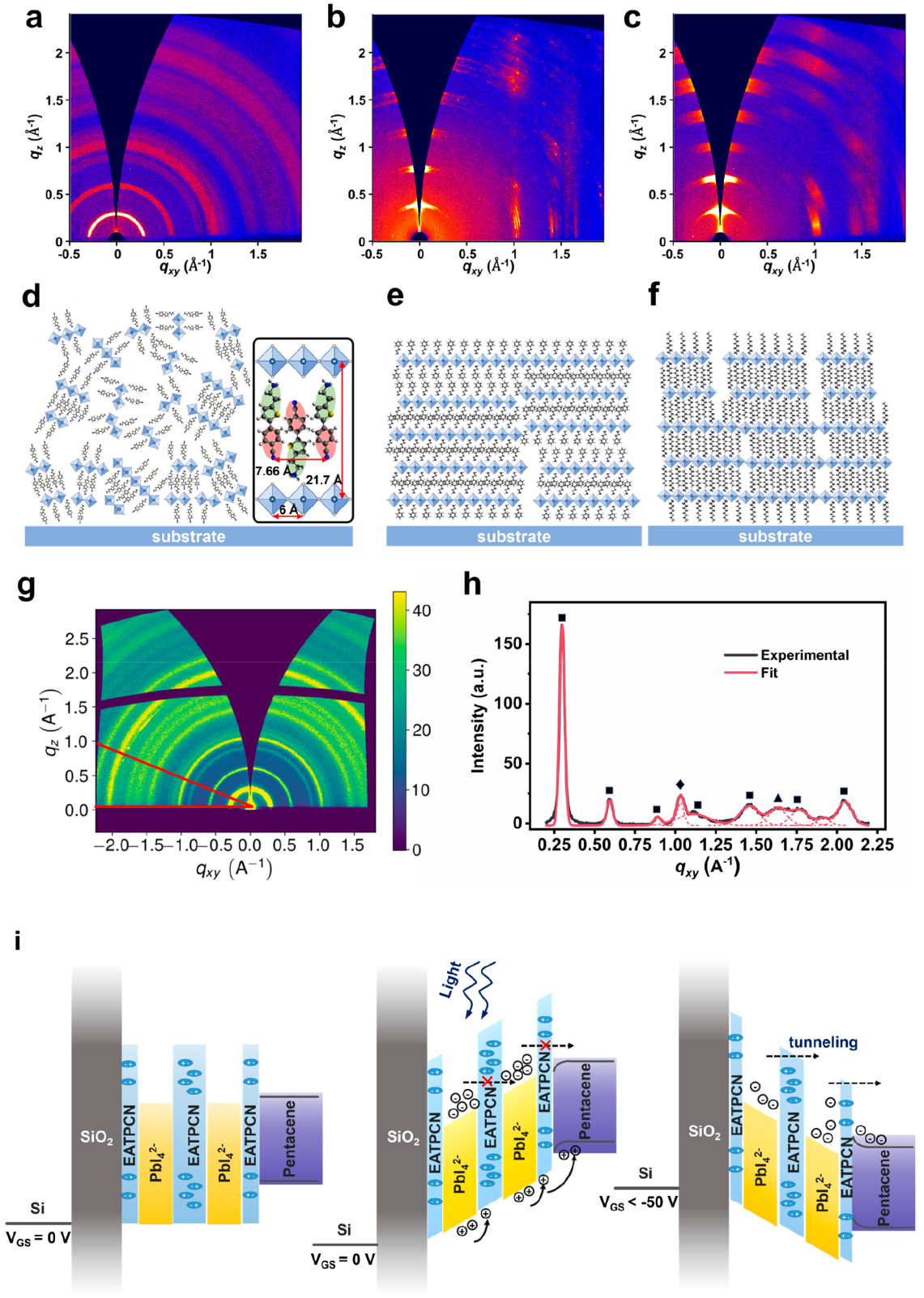

Figure 2. GIWAXS measurements and molecular arrangements of 2D perovskites, as well as operation mechanisms of $(EATPCN)_2PbI_4$ photomemristors. GIWAXS patterns of (a) $(EATPCN)_2PbI_4$, (b) $(PEA)_2PbI_4$, and (c) $(OA)_2PbI_4$ films. All of them display strong peaks at the crystalline direction of (002) and (004). Crystal alignments of various 2D perovskite extracted from the GIWAXS patterns. (d) $(EATPCN)_2PbI_4$ exhibits a random crystal orientation; (e) $(PEA)_2PbI_4$ and (f) $(OA)_2PbI_4$ show neatly arranged crystal structures parallel to substrates. The inset of (d) is the detailed molecular arrangement of $(EATPCN)_2PbI_4$ and the push−pull structure of EATPCN with the thiophene, and the benzonitrile group prevents $(EATPCN)_2PbI_4$ from forming a long-period crystalline structure. (g) High signal-to-noise ratio GIWAXS pattern of $(EATPCN)_2PbI_4$. (h) Integrated intensity along q_{xy} of $(EATPCN)_2PbI_4$ film from cake cut marked in (g). The

https://doi.org/10.1021/acsnano.3c09595
ACS Nano 2023, 17, 25552−25564

Figure 2. continued

rectangle, diamond, and triangle symbols correspond to the diffraction signals from 2D perovskite stacking, PbI_4^{2-} octahedra, and possible $\pi-\pi$ stacking, respectively. (i) Proposed operation mechanism of $(EATPCN)_2PbI_4$ photomemristors. The left is the original energy band alignment of $(EATPCN)_2PbI_4$ transistors. The middle means excitons generated at PbI_4^{2-} layers under irradiation. Holes move away along the band alignment and electrons are trapped. The right means that trapped electrons tend to tunnel out to pentacene or recombine with the holes injected from the pentacene layer.

52.4% quenched, respectively. However, only the 30.9% PL intensity of $(OA)_2PbI_4$ is quenched, indicating its retarded charge transfer. The time-resolved photoluminescence (TRPL) results, as depicted in Figure S5, also reveal a more pronounced change in lifetime for $(EATPCN)_2PbI_4$ and $(PEA)_2PbI_4$ samples compared to that of the $(OA)_2PbI_4$ sample, consistent with the photoluminescence intensity results. Effective charge transfer means that more holes are efficiently extracted from the perovskite to pentacene, reducing the recombination probabilities and increasing the device sensitivity upon light stimuli. The scanning transmission electron microscope (STEM) images of various perovskites are shown in Figure 1g and Figure S6. $(EATPCN)_2PbI_4$, $(PEA)_2PbI_4$, and $(OA)_2PbI_4$ possess distinctly different appearances. However, all of them do not exhibit obvious lattice fringe under TEM inspection, in contrast to $MAPbI_3$, which exhibits clear lattice fringe.[28] The atomic force microscopy (AFM) images of the perovskite films are shown in Figure 1h. The $(EATPCN)_2PbI_4$ AFM image is consistent with its STEM image and displays a much smoother morphology (R_q = 0.279 nm) than those of the other samples. Additionally, the grain size of $(EATPCN)_2PbI_4$ is much smaller and better dispersed, which is also consistent with the results of X-ray diffraction (XRD) shown in Figure 1e. Figure 1i shows the AFM images of pentacene deposited on perovskite. Owing to the much smoother surface of the $(EATPCN)_2PbI_4$ underlayer, the pentacene grain on $(EATPCN)_2PbI_4$ appears larger than those on top of 2D $(PEA)_2PbI_4$ and $(OA)_2PbI_4$ as well as 3D $MAPbI_3$, which is advantageous for improving the electrical performance and enhancing the charge carrier mobility of pentacene.

Spatial Crystal Arrangement and Energetic Band Alignment. GIWAXS measurements were conducted to analyze the perovskite crystal packing and orientation with various cations. As shown in Figure 2a–c, $(PEA)_2PbI_4$ and $(OA)_2PbI_4$ display strong signals along the q_z direction, representing the crystalline direction of (002) and (004), indicating the preferred crystal orientation in the direction parallel to the substrate. However, in contrast to commonly observed 2D RP perovskites, there is no significant preferred crystal orientation observed in $(EATPCN)_2PbI_4$, even though it forms a 2D perovskite.[29] The q values of $(EATPCN)_2PbI_4$, $(PEA)_2PbI_4$, and $(OA)_2PbI_4$ corresponding to (002) and (004) planes are 0.29 and 0.59 $Å^{-1}$, 0.39 and 0.79 $Å^{-1}$, and 0.34 and 0.68 $Å^{-1}$ respectively, as shown in Figure S7. The q values of $(EATPCN)_2PbI_4$ are significantly smaller than those of $(PEA)_2PbI_4$ and $(OA)_2PbI_4$, indicating an increase of interplanar spacing in $(EATPCN)_2PbI_4$. Figure 2d–f illustrates the proposed perovskite crystal stacking orientation of various 2D perovskites. Both $(PEA)_2PbI_4$ and $(OA)_2PbI_4$ exhibit crystal structures that are mostly parallel to the substrates. In contrast, $(EATPCN)_2PbI_4$ exhibits random crystal orientation, resulting in the absence of a long-order 2D perovskite structure that hinders effective charge carrier transport. We believe this isotropic orientation is important for device memory retention, as it largely prevents the escape of trapped carriers. Due to the significantly bigger stacking distances obtained from XRD and GIWAXS observed in the $(EATPCN)_2PbI_4$ thin film, we conducted further GIWAXS measurements to obtain more detailed information about its nanostacking. The results are presented in Figure 2g and 2h. The $(EATPCN)_2PbI_4$ film exhibits a clear isotropic crystal orientation. Figure 2h displays the integrated intensity along the direction parallel to the substrate (cake cut marked in red in Figure 2g). The prominent peak observed at 0.29 $Å^{-1}$, along with its periodic higher order diffractions, corresponds to the interfacial spacing (d-spacing) of 21.7 Å. This peak is attributed to the PbI_4^{2-} layer structure, which aligns with the XRD result of approximately 20.9 Å. The much larger spacing between PbI_4^{2-} layers (21.7 Å) compared with $(PEA)_2PbI_4$ and $(OA)_2PbI_4$ (16.1 and 18.5 Å, respectively, from GIWAXS; 16.2 and 18.6 Å, respectively, from XRD) correlates with the retarded charge transport between the adjacent perovskite crystals. Inspired by the work of Park's group,[30] we propose the molecular arrangement of organic cations between PbI_4^{2-} layers, as shown in Figure S8. The calculated molecular length of EATPCN is 11.51 Å. The observed d-spacing of 21.7 Å suggests that the EATPCN intercalates between the two PbI_4^{2-} layers partially overlapping. From Figure 2g and 2h, in conjunction with GIWAXS information on the EATPCNI molecule neat film (Figure S9), we can determine that in $(EATPCN)_2PbI_4$ thin films, the Pb–Pb distance is about 6 Å based on the peak at 1.04 $Å^{-1}$. Additionally, the intermolecular distance (possible $\pi-\pi$ interaction distance) between EATPCN and EATPCN is determined to be 3.83 Å based on the peak at 1.64 $Å^{-1}$. The experimentally observed $\pi-\pi$ stacking distances of EATPCN and EATPCN agree well with the theoretical calculations (Figure S10). The dipolar nature of the aromatic block in the EATPCN molecule leads to an antiparallel dimeric alignment, with an intermolecular distance of 3.7 Å, which closely matches the observed value of 3.83 Å in GIWAXS. The calculated distance between the two amino anchors of this dimeric pair is around 16 Å. Taking into consideration the binding distance between organic molecules and Pb, this result aligns with the observed d-spacing between two PbI_4^{2-} octahedral layers (20.9 Å from XRD and 21.7 Å from GIWAXS). As a result, with the amine groups of EATPCN anchoring to PbI_4^{2-}, the dipole–dipole and $\pi-\pi$ interactions between two neighboring ligands lead to an increase of interlayer distance. The effective distance between two ligands anchoring to the same side of PbI_4^{2-} is twice that of the measured 3.83 Å, which is 7.66 Å. This distance is significantly larger than the measured Pb–Pb distance of 6 Å. Due to this mismatch in distances (6 Å vs 7.66 Å), we believe that the perovskite material is more prone to have disordered arrangements. Accordingly, it becomes more challenging to form a long-range and well-defined crystal structure in the $(EATPCN)_2PbI_4$ film, as indicated by the significantly broader diffraction peaks observed in the XRD measurements in comparison to the other two materials. The disordered nature

https://doi.org/10.1021/acsnano.3c09595
ACS Nano 2023, 17, 25552–25564

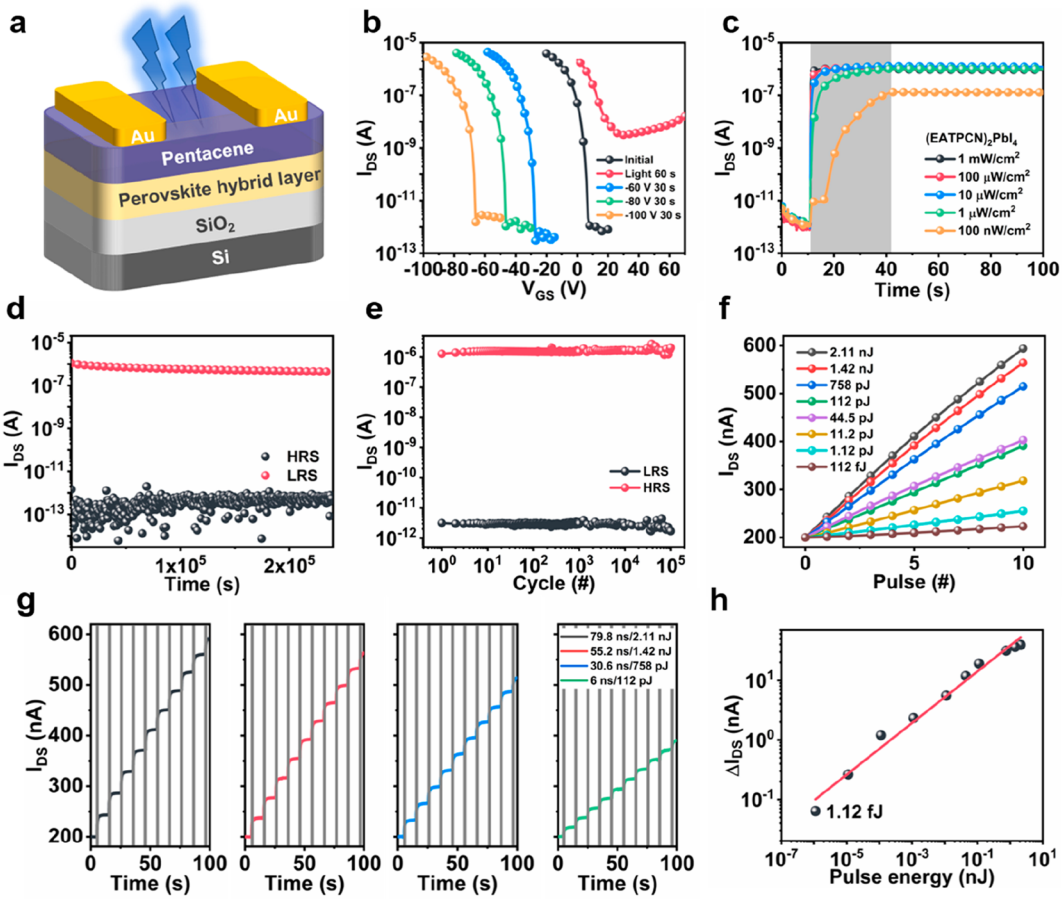

Figure 3. Device characterizations of $(EATPCN)_2PbI_4$ photomemristors. (a) Schematic representation of the device structure with a perovskite hybrid layer as the trapping layer to induce a channel in pentacene. (b) Transfer characteristics of $(EATPCN)_2PbI_4$ transistors. The light stimulation with an intensity of 1 mW/cm^2 for 60 s is plotted as a red line, and the negative biases of −60 V (blue line), −80 V (green line), and −100 V (orange line) for 30 s were used. (c) Temporal response of $(EATPCN)_2PbI_4$ transistors with 365 nm light with intensity ranging from 1 mW/cm^2 to 100 nW/cm^2 for 30 s. (d) Retention time measurement of $(EATPCN)_2PbI_4$ transistors with an on/off ratio of 10^{6-7} over 2.4 × 10^5 s. (e) Endurance measurement using 365 nm light (1 mW/cm^2) and −80 V for 300 ms as potentiation and depression stimulus. An on/off ratio of around 10^6 remains unchanged after 10^5 WRER cycles. (f) The linear I_{DS} change of $(EATPCN)_2PbI_4$ devices performed by a nanosecond pulsed laser with the pulse energy ranging from 2.11 nJ to 112 fJ. (g) The detailed I_{DS} change of $(EATPCN)_2PbI_4$ devices with the pulse energy ranging from 2.11 nJ to 112 pJ. (h) The ΔI_{DS} to pulse energy ranging from 2.11 nJ to 1.12 fJ. The lowest energy consumption of 1.12 fJ is shown.

and much smaller crystal size of the $(EATPCN)_2PbI_4$ layer offer morphological advantages for indefinite electron trapping, resulting in an almost zero-decay nonvolatile property (*vide infra*).

In contrast to the common 2D RP perovskite with nonpolar organic cations and 3D perovskite, utilizing 2D $(EATPCN)_2PbI_4$ as trapping layer in the photomemristor offers twofold advantages energetically and morphologically. The HOMO level of EATPCNI was determined to be −5.92 eV by an ultraviolet photoelectron spectroscopy (UPS) measurement. With the optical bandgap of the materials, the LUMO level of EATPCNI was calculated to be around −2.38 eV (Figure S11a). Similarly, the valence band level of PbI_4^{2-} measured by UPS was fitted to be −5.93 eV (Figure S11b), and the conduction band level was calculated to be around −3.56 eV, similar to the previously reported values.[31] The LUMO and HOMO of pentacene are well-known to be around −3.2 and −5.0 eV, respectively.[22] With these values, the energy level alignment is depicted in Figure 2i. Upon light stimulation, photoinduced electron−hole pairs are generated in the PbI_4^{2-} layers. As the charges dissociate, the holes tend to move away from the PbI_4^{2-} layer along the band alignment, while the electrons are inclined to be trapped in the PbI_4^{2-} layers. The push−pull structure of EATPCN introduces a HOMO level that is almost aligned with the valence level of PbI_4^{2-} and slightly deeper-lying compared to the HOMO level of pentacene. Also, with its high dipole moment, EATPCN and the resulting antiparallel packing of EATPCN−EATPCN make it a good hole transport medium.[32] In contrast, most of the organic cations of 2D RP perovskites exhibit a much lower-lying HOMO level. For instance, it has been reported that the HOMO/LUMO levels of PEA are −7.70/−2.40 eV.[25] While electrons can naturally be trapped in PbI_4^{2-} layers, extracting holes to pentacene is difficult because the very low-lying HOMO level of PEA renders a high interface energy barrier. This unmatched energy level alignment eventually leads to the recombination of electron−hole pairs, causing any memory effect to vanish and resulting in low light sensitivity and volatile characteristics. The energy barrier formed by the LUMO difference endows $(EATPCN)_2PbI_4$ devices with a long-term

https://doi.org/10.1021/acsnano.3c09595
ACS Nano 2023, 17, 25552−25564

retention ability. When a large amplitude of negative bias, typically lower than −50 V, is applied to $(EATPCN)_2PbI_4$ devices, it effectively causes band bending, enabling trapped electrons to tunnel away from the PbI_4^{2-} layer and facilitating their recombination with holes injected from the pentacene layer.

Photomemristor Characterizations. The $(EATPCN)_2PbI_4$ was subsequently utilized as a charge-trapping floating-gate layer in photomemristors. The device configuration is shown in Figure 3a, featuring a bottom gate and top contact configuration and using highly doped Si and 300 nm SiO_2 as the gate electrode and gate oxide, respectively. The transfer characteristics of the $(EATPCN)_2PbI_4$ devices are shown in Figure 3b. The black line represents the initial state, and the devices were then biased with a negative gate to source voltage (V_{GS}) bias (V_{GS} = −60, −80, and −100 V) and ultraviolet light illumination (365 nm, 1 mW/cm^2). The threshold voltage (V_{th}) of the device shifted positively to 14.9 V after light irradiation. This indicates that electrons can be effectively stored in the perovskite trapping layer, inducing a hole channel in pentacene and causing the device to become a normally on transistor. Furthermore, when a negative gate bias was applied, V_{th} was shifted to −33.4, −52.5, and −73.0 V with V_{GS} = −60, −80, and −100 V of negative bias, respectively. This phenomenon suggests that trapped electrons can be removed by tunneling, swept out by the negative bias, or recombined with holes injected from the pentacene channel. As a result, $(EATPCN)_2PbI_4$ devices showed an extraordinarily large memory window of 87.9 V.

The temporal response of drain to source current (I_{DS}) of devices illuminated with 365 nm light at intensities ranging from 1 mW/cm^2 to 100 nW/cm^2 for 30 s is shown in Figure 3c and Figure S12. V_{GS} = 0 V and V_{DS} = −5 V are applied in the reading process throughout the entire study. Initially, the I_{DS} of $(EATPCN)_2PbI_4$ devices is in a high-resistance state (HRS) with a low current of 10^{-12} A. When illuminating $(EATPCN)_2PbI_4$ devices with a light intensity above 1 μW/cm^2, the I_{DS} increases immediately and is saturated at ∼10^{-6} A. Under a weaker light intensity of 100 nW/cm^2, the I_{DS} increases gradually. It is worth noting that the I_{DS} remains at the same level when the illumination was turned off, implying that $(EATPCN)_2PbI_4$ devices possess an outstanding retention ability. It is worthy to note that $(PEA)_2PbI_4$ devices behave similarly to the $(EATPCN)_2PbI_4$ devices, except for much inferior retention performance. Furthermore, $(OA)_2PbI_4$ and $MAPbI_3$ devices show volatile characteristics not only in the HRS but also in the low-resistance state (LRS), even though their I_{DS} stays at higher levels with an increase in the light intensity. Some researchers regard this initial drop in memory state as the oblivion of short-term memory and the final stabilized state as long-term memory.[33] Although it is possible to find some special applications that utilize these decay characteristics of the memristors, the complex decayed volatile behavior and the lengthy time constants hinder the versatile and high-speed advantages of memristors in neuromorphic computing.

We examined the detailed retention ability of $(EATPCN)_2PbI_4$ devices, and the results are shown in Figure 3d. Both HRS and LRS display negligible changes after 2.4 × 1 × 10^5 s. Considering both short-term and long-term results, it is indicated that $(EATPCN)_2PbI_4$ devices are able to effectively maintain their resistance states after stimulations without an initial drop and keep the nonvolatile memory state for a very long period of time. The writing−reading−erasing−reading (WRER) measurement was also employed to examine the endurance of the $(EATPCN)_2PbI_4$ devices. In the fully-on-and-fully-off writing and erasing procedures, 365 nm light with a light intensity of 1 mW/cm^2 and V_{GS} = −80 V were utilized to fully potentiate and fully depress the device, respectively. As shown in Figure 3e, exceptional reliability of $(EATPCN)_2PbI_4$ devices is demonstrated, with an on/off ratio of ∼10^6 maintained after 10^5 programming cycles. It is noteworthy that this kind of endurance is among the best reported performance in transistor-type floating-gate photomemristors realized by any material systems, including perovskites, 2D transition metal dichalcogenides, and organic semiconductors.[3,34−36]

The energy consumption is also a crucial parameter in evaluating the performance of photomemristors. In this study, we comprehensively consider both the energy consumption of a single applied light stimulus pulse and the energy consumption during the reading process, as described in the following equations:[37]

$$dE_{write} = P \times S \times dt \quad (1)$$

$$dE_{read} = V \times I \times dt \quad (2)$$

In eq 1, P, S, and dt represent the power consumption per unit area, active area, and the duration of the light pulse, respectively. The equation describes the energy consumption for each memory state update. In eq 2, V, I, and dt represent the reading drain-to-source voltage, the drain-to-source current, and the duration of the reading current pulse, respectively. The equation represents the energy consumption of reading the status of the memristor. The width of the light pulse ranged from 6 to 129 ns, which corresponds to a pulse energy ranging from 4.46 to 140.4 nJ. We not only employed the narrowest pulse width to examine the resistance states of devices but also attenuated the pulse intensity to inspect its lowest response limit. When illuminated by the pulse light, the I_{DS} of $(EATPCN)_2PbI_4$ devices presented a linear increase, as shown in Figure 3f and 3g. The extracted ΔI_{DS} corresponding to the pulse energy is plotted in Figure 3h, showing that $(EATPCN)_2PbI_4$ devices can effectively respond to the irradiated energy within the extremely narrow pulse width of up to 6 ns. As a result, the energy consumption of the light stimulation was determined to be very low, at 1.12 fJ, and the reading energy consumption during the process was calculated to be merely 6 fJ. The low energy consumption required for a single memory state update of $(EATPCN)_2PbI_4$ devices indicates a cost advantage in large-scale parallel computing.[38] Furthermore, the superhigh sensitivity, coupled with its persistent nonvolatile characteristics, suggests that $(EATPCN)_2PbI_4$ devices also have a promising application as a stand-alone, single-device-based energy meter capable of detecting pulse energy at the femtojoule level, in contrast to their conventional use as power meters. This differs from the common practice of employing a photodiode as an energy meter, which can only measure instantaneous light intensity power and necessitates a circuit for continuous readings and photocurrent integration in order to calculate the light energy. The sensitivity of the $(EATPCN)_2PbI_4$ devices surpasses that of commercial state-of-the-art pulse energy sensors by several orders of magnitude. For instance, the lowest detection limit of Ophir PD-10-pJ-C is as high as 200 pJ.

https://doi.org/10.1021/acsnano.3c09595
ACS Nano 2023, 17, 25552−25564

Table 1. Characteristics of Floating-Gate Transistors Previously Reported and Reported Herein

material	on/off	memory window (V)	retention (s)	endurance (cycles)	power consumption	memory capacity (bit)	decay after 10^3 s (%)	ref
P2VP/$MAPbBr_3$/pentacene	10^5		10^4	100			>50	47
P3HT/$CsPbBr_3$	10^5				0.18 fJ		>60	35
OS/$Cs_2AgBiBr_6$/IDTBT	10^5	58	10^4	20			>50	48
PMMA/PCBM/Pentacene	10^4	22.1	1.2×10^4	800		2	>50	49
PS/$CsPbBr_3$/pentacene	10^7	~90	10^4			2	>70	36
$(PEA)_2PbBr_4$/C8-BTBT	10^4	>180	10^4	10^4			>20	25
PS/$CsPbBr_3$/PCBM/pentacene	10^3	32.8	10^4	500			~ 50	50
$(BA)_2MAPb_4I_7$/hBN/MoS_2	10^4	92	10^3	1000	36 pJ/10 pJ	>4	>80	51
$(BA)_2MAPb_4I_7$/MoS_2	10^4	104	10^3	10^3	5.1 pJ	>6	>50	52
$(EATPCN)_2PbI_4$/pentacene	10^6	87.9	2.4×10^5	10^5	1.12 fJ/6 fJ	~8	3.44	this work

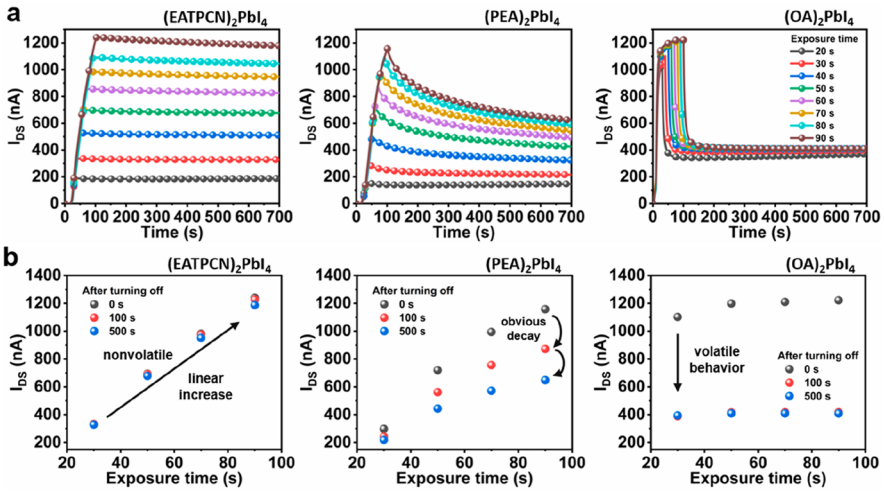

Figure 4. Characterization of multistate memory and retention time in 2D perovskite-based photomemristors. (a) I_{DS} variation of $(EATPCN)_2PbI_4$ transistors (left), $(PEA)_2PbI_4$ transistors (middle), and $(OA)_2PbI_4$ transistors (right) using 365 nm light with an intensity of 100 nW/cm^2 for the exposure time ranging from 20 to 90 s. (b) I_{DS} values of $(EATPCN)_2PbI_4$ transistors (left), $(PEA)_2PbI_4$ transistors (middle), and $(OA)_2PbI_4$ transistors (right) with different exposure times. Black, red, and blue symbols represent I_{DS} values after turning off the light.

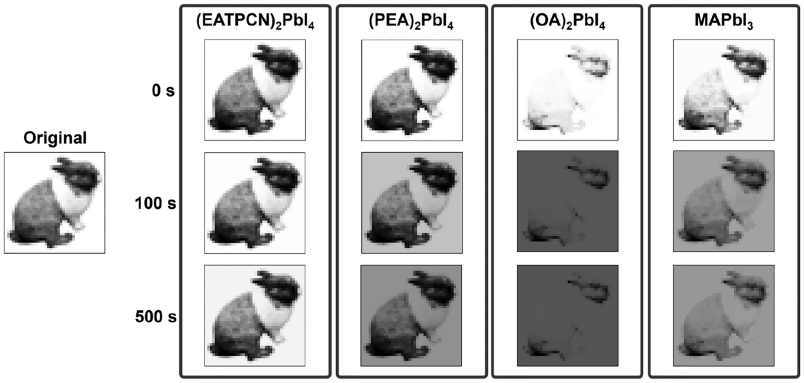

Figure 5. Reconstruction of rabbit images using perovskite-based photomemristors and their temporal variations. A rabbit image rebuilt by the multilevel I_{DS} values of $(EATPCN)_2PbI_4$, $(PEA)_2PbI_4$, $(OA)_2PbI_4$, and $MAPbI_3$ transistors after turning off the light for 0, 100, and 500 s. $(EATPCN)_2PbI_4$ transistors accurately represent the original image and remain unchanged after 500 s. $(OA)_2PbI_4$ and $MAPbI_3$ transistors cannot represent the original image and quickly fade out over time.

A detailed comparison of important indices in the field of floating-gate transistors is given in Table 1. $(EATPCN)_2PbI_4$ photomemristors perform much better than most of the previous works in nearly every index. The endurance stability and memory storage capacity are far superior to those in most reports. Although other works have reported lower reading energy consumption, the energy consumption of light stimulus is still much larger (~nJ),[37] which highlights the advantage in light sensitivity of $(EATPCN)_2PbI_4$ photomemristors. More importantly, the table also highlights the decay percentage of

https://doi.org/10.1021/acsnano.3c09595
ACS Nano 2023, 17, 25552−25564

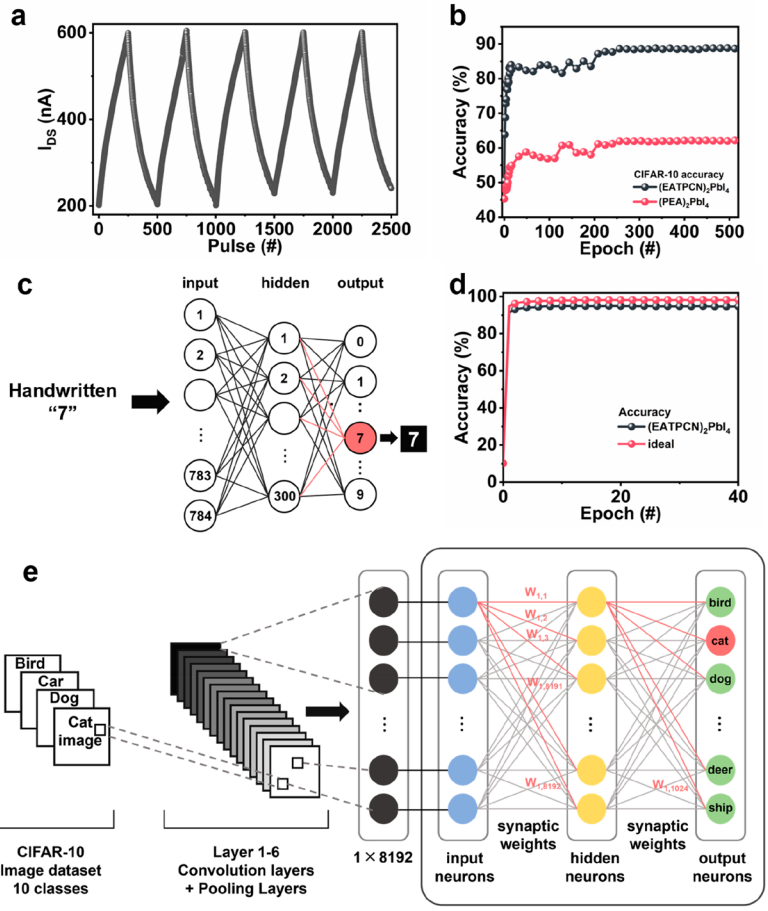

Figure 6. Multilevel memory performance of $(EATPCN)_2PbI_4$ photomemristors and their application in neuromorphic computing. (a) Repetitive potentiation and depression operation of $(EATPCN)_2PbI_4$ transistors by 250 pulses of 365 nm light (6.62 nm/cm^2) and −17.5 V for 500 ms. (b) Recognition accuracies of $(EATPCN)_2PbI_4$ photomemristors for the CIFAR-10 data set for 512 epochs. (c) Neural networks for MNIST handwritten digit recognition tasks. (d) Recognition accuracies of $(EATPCN)_2PbI_4$ and $(PEA)_2PbI_4$ photomemristors for an MNIST handwritten data set for 40 epochs. (e) DNN+ NeuroSim convolutional neural networks for CIFAR-10 recognition, including convolution layers and pooling layers (layers 1−6), and fully interconnected layers for the training of synaptic weights.

all reported photomemristors after a long period of time of 1000 s. Our $(EATPCN)_2PbI_4$ photomemristors exhibit much smaller decay, with percentages 1 to 2 orders of magnitude lower than those of all other devices. The reproducibility of $(EATPCN)_2PbI_4$ photomemristors was assessed by fabricating 15 devices on five different substrates, resulting in a 100% success rate and minimal device variation, as shown in Figure S13.

Multistate Memory Characterization of Perovskite-Based Photomemristors. Figure 4a and Figure S14a demonstrate the variation of the I_{DS} values of four types of devices illuminated with stimulation light. The I_{DS} of $(EATPCN)_2PbI_4$ devices increases linearly from 187 to 1241 nA with the exposure time. The $(PEA)_2PbI_4$ devices also exhibit a linear increase in I_{DS} from 167 to 1157 nA. However, the I_{DS} of $(OA)_2PbI_4$ and $MAPbI_3$ saturate rapidly, showing only slight growth with increasing exposure time. To compare the retention abilities, Figure 4b and Figure S14b display the I_{DS} of varying exposure times after turning off the light. The I_{DS} of $(EATPCN)_2PbI_4$ devices shows negligible current decay after turning off the light stimulus for 100 and 500 s, respectively, while the I_{DS} of $(PEA)_2PbI_4$ devices shows a noticeable drop of 22.0% and 38.3%, respectively. In sharp contrast, devices based on $(OA)_2PbI_4$ and $MAPbI_3$ show much worse performances, in terms of linearity of I_{DS} or the retention ability. With the time-dependent I_{DS} values of the actual devices, we rebuilt a rabbit image, as shown in Figure 5. First, 8 values of I_{DS} corresponding to 8 exposure times are interpolated to 256 levels. The image is grayscaled and rebuilt using the normalized I_{DS} from 0 to 1 for each device. As displayed in Figure 5, $(EATPCN)_2PbI_4$ and $(PEA)_2PbI_4$ can faithfully render the image, while $(OA)_2PbI_4$ and $MAPbI_3$ rather appear to have color discrepancies in terms of lightness due to their high nonlinearity of the I_{DS}. Furthermore, the images of devices employing $(PEA)_2PbI_4$, $(OA)_2PbI_4$, and $MAPbI_3$ became darker over time, causing the images to lose fidelity. In contrast, the images of the $(EATPCN)_2PbI_4$ device still remain unchanged, which is a result of the exceptional retention ability of the $(EATPCN)_2PbI_4$ devices.

Applications of $(EATPCN)_2PbI_4$ Photomemristors in Neuromorphic Computing. The multilevel memory performance of the $(EATPCN)_2PbI_4$ devices was examined, and the results are shown in Figure 6a. A total of 250 pulses of equal-intensity and equal-duration light, along with a sequence of equal-voltage and equal-duration negative V_{GS} bias, were utilized as stimuli for potentiation and depression, respectively. Intriguingly, every conductance state could be clearly distinguished, indicating that our $(EATPCN)_2PbI_4$ devices

https://doi.org/10.1021/acsnano.3c09595
ACS Nano 2023, 17, 25552−25564

could achieve ~8 bits of multibit capacity. The exceptional memory capacity of $(EATPCN)_2PbI_4$ devices can be reasonably attributed to their ultrahigh light sensitivity, which endows them with numerous distinguishable nonvolatile states. The nonlinearity values are found to be 0.92 and 2.58 for potentiation and depression, respectively. We then implemented our $(EATPCN)_2PbI_4$ devices into the image recognition of the CIFAR-10 data set through the DNN+ NeuroSim simulator. The CIFAR-10 data set comprises 60 000 color images, with each image containing three color channels (red, green, and blue) and a size of 32 × 32 pixels. These images are divided into 10 different classes, such as airplanes, ships, dogs, and more. The data set is further split into a training set consisting of 50 000 images and a test set consisting of 10 000 images. Within each class, there are 5000 images for training and 1000 images for testing purposes. The detailed process of CIFAR-10 recognition through DNN+ NeuroSim is illustrated in Figure 6e. In the DNN+ NeuroSim simulator, we use the default VGG-8 network for our model. VGG-8 is a convolutional neural network (CNN) architecture consisting of six convolutional layers and two fully connected layers.[39,40] The information on $(EATPCN)_2PbI_4$ devices such as nonlinearity and conductance states was implemented into the synaptic weights between input, hidden, and output layers; the synaptic weights were modulated during the operation of feed-forward and back-propagation. During each epoch, 50 000 training images and 10 000 testing images were utilized. Consequently, a recognition accuracy of 89% was achieved after 512 epochs, which is comparable to both the experimental results and the ideal ones reported by other groups.[41] For comparison, we also applied $(PEA)_2PbI_4$ devices into the CIFAR-10 recognition task, resulting in a much lower accuracy of 62%, as shown in Figure 6b. Additionally, we applied a handwritten digit data set from the MNIST database to the recognition tasks, as shown in Figure 6c.[42] The classification accuracy reached an unparalleled 94.8% after only 40 epochs, compared to other works, which achieved 90% accuracy,[43] as shown in Figure 6d. High linearity and a large number of conduction states are key factors for analogue tuning in recognition tasks during the back-propagation process, leading $(EATPCN)_2PbI_4$ devices to exhibit outstanding performance. The exceptional classification accuracy achieved through the use of $(EATPCN)_2PbI_4$ devices in the two recognition tasks suggests great potential for the universal applicability of our innovative $(EATPCN)_2PbI_4$ 2D RP perovskite as computing elements in neuromorphic systems.

CONCLUSION

In summary, a push−pull donor−acceptor-configured organic cation was designed specifically for 2D perovskite-based photomemristor applications. High-performance photomemristors were fabricated and characterized with 2D $(EATPCN)_2PbI_4$ perovskite as trapping layers along with the $(PEA)_2PbI_4$, $(OA)_2PbI_4$, and $MAPbI_3$ devices for comparison. The results indicate that $(EATPCN)_2PbI_4$ photomemristors possess a very wide memory window of 87.9 V and an on/off ratio of 10^6 with a retention time more than 2.4×10^5 s. More importantly, device endurance was examined through fully-on-fully-off WRER measurement, demonstrating an on/off ratio of around 10^6 after 10^5 cycles. The devices also showed excellent low memory state update and read energy consumption of 1.12 and 6 fJ, respectively. In addition, the ability to rebuild a rabbit image using multilevel I_{DS} values was demonstrated and showed that the image of $(EATPCN)_2PbI_4$ devices accurately represented the original appearance of the photo, displaying no changes after a long period time of 500 s. These results showcase the outstanding linearity and almost zero-decay retention ability of $(EATPCN)_2PbI_4$ photomemristors. The excellent performance is attributed to the donor−acceptor-type push−pull organic cation, which provides nearly perfect energy level and morphology conditions simultaneously. These conditions are extremely difficult, if not impossible, to realize with traditional 2D RP perovskites or 3D perovskites. Lastly, clearly distinguishable ~8 bits of memory states that could be linearly potentiated and depressed, respectively, by a sequence of identical light pulses and voltage pulses were demonstrated. By utilizing the devices in the recognition tasks, excellent accuracies of 89% and 94.8% were reached for CIFAR-10 and the handwritten digit data set from the MNIST database, respectively, indicating the exciting potential of utilizing these truly nonvolatile multilevel perovskite photomemristors for future hardware-based photonic neuromorphic computing.

METHODS

Materials. Phenethylammonium iodide (PEAI), *n*-octylammonium iodide (OAI), and methylammonium iodide (MAI) were purchased from Greatcell Solar Materials (Australia). *N*,*N*-Dimethylformamide (DMF, anhydrous, 99.8%) and poly(methyl methacrylate) (PMMA, average M_w ~ 15 000) were purchased from Sigma-Aldrich (Missouri, USA). Lead iodide (PbI_2) and pentacene (purified by sublimation) were purchased from Tokyo Chemical Industry Co., Ltd. (TCI).

Device Fabrication. Highly doped p-type silicon wafers with a 300 nm SiO_2 dielectric layer were cleaned in sequence with detergent, deionized water, acetone, and methanol. The solution of the perovskite trapping layer was prepared by mixing EATPCNI, PbI_2, and PMMA in DMF with a concentration of 104 mg mL^{-1} (EATPCNI:PbI_2 (molar ratio) = 2:1, perovskite:PMMA (weight ratio) = 25:1). The solution was then spin-coated at 3000 rpm for 60 s on the precleaned substrates and annealed at 100 °C for 5 min. The thicknesses of the perovskite layers were ~60 nm. The samples were transferred to a high-vacuum chamber (base pressure: ca. 2×10^{-6} Torr) for deposition of 50 nm pentacene and 50 nm Au electrodes. The pentacene was thermally deposited at a rate of 0.15 nm s^{-1}. The gold electrode was deposited onto pentacene with a shadow mask with a channel length of 50 μm and a channel width of 1000 μm, respectively.

Device Characterization. The electrical characteristics of the devices were measured using a Keithley 2636A SourceMeter and a Keysight B1500A semiconductor parameter analyzer. The absorption spectra for the perovskite trapping layers were recorded using a Shimadzu UV-2600 spectrophotometer. The PL spectra were recorded using a charge-coupled device (CCD) camera (PIX-IS256BR, Princeton Instruments) in a front-face configuration and pumped by a 375 nm diode laser. Transient PL was measured using a photon-counting photomultiplier tube. The excitation source was a pulsed diode laser (λ = 375 nm; PicoQuant). The photon counts were recorded using a time-correlated single-photon-counting module (SPC-130-EM, Becker & Hickl). The thicknesses of the perovskite layers were determined using spectroscopic ellipsometry (J. A. Woollam, V-VASE). XRD was conducted using a Bruker D2 PHASER with Cu Kα radiation. AFM images were obtained using a scanning probe microscope (Bruker, model: Dimension ICON). XPS and UPS information were acquired using electron spectroscopy for chemical analysis (ULVAC-PHI, PHI 5000 Versaprobe II). TEM and STEM images were recorded using a spherical-aberration-corrected field-emission transmission electron microscope (Cs-corrected TEM, JEOL ARM-200FTH) at an accelerating voltage of 200 kV. Energy consumption measurements with a nanosecond pulse width were obtained using a nanosecond pulsed laser diode system (NPL41C,

https://doi.org/10.1021/acsnano.3c09595
ACS Nano 2023, 17, 25552−25564

Thorlabs). GIWAXS measurements of Figure 2a–c and Figure S7 were conducted at beamline 23A1 (BL 23A1) at National Synchrotron Radiation Research Center (NSRRC) in Taiwan.[44−46] The GIWAXS measurements were performed using a monochromatic X-ray beam with a wavelength of 1.2398 Å at an incident angle of 0.2°. The scattering signals were collected by a flat-panel detector (C10158DK with 2352 pixels), where the distance between the sample and the detector was 19.6 cm and the collection time was 10 s for each measurement. GIWAXS measurements of Figures 2g and 2h and S9 were performed using a Xeuss 3.0 (Xenocs, France) equipped with a copper source (λ = 1.5418 Å). Scattering images were detected on an Eiger2 R 1M detector (Dectris, Switzerland) with 1028 × 1062 pixels and a pixel size of 75 μm × 75 μm located 72 mm from the sample (deduced via AgBeh calibration). The beam size was adjusted to 0.5 × 0.5 mm with an incidence angle of 0.4°, and each sample was measured for 4 h in vacuum, with 4 single-image exposure times of 60 min. The measured single GIWAXS images were averaged and missing wedge corrected using XSACT 2.0 (Xenocs, France). The theoretical simulation was performed with the Gaussian 16 program package. The geometry optimization of both EATPCN (monomer) and $(EATPCN)_2$ (dimer) was conducted with density functional theory (DFT) at the ωB97X-D/6-31G(d,p) level. The initial guess of the dimer geometry is based on the GIWAXS result in this work and our previous studies (Supporting Information), where the two molecules were stacked in antiparallel form separated by an $\pi-\pi$ interaction distance (0.35 nm).

ASSOCIATED CONTENT

Supporting Information

The Supporting Information is available free of charge at https://pubs.acs.org/doi/10.1021/acsnano.3c09595.

Synthetic process of the EATPCNI molecule and its NMR spectra; STEM and GIWAXS information on perovskite films; theoretical simulation of optimized molecular $(EATPCN)_2$ dimer; temporal response and multilevel drain current variation of perovskite photomemristors (PDF)

AUTHOR INFORMATION

Corresponding Authors

Ken-Tsung Wong − *Department of Chemistry, National Taiwan University, Taipei 10617, Taiwan; Department of Chemistry, National Taiwan University, Taipei 10617, Taiwan;* orcid.org/0000-0002-1680-6186; Email: kenwong@ntu.edu.tw

Hao-Wu Lin − *Department of Materials Science and Engineering, National Tsing Hua University, Hsinchu 30013, Taiwan; Frontier Research Center on Fundamental and Applied Sciences of Matters, National Tsing Hua University, Hsinchu 30013, Taiwan;* orcid.org/0000-0003-4216-7995; Email: hwlin@mx.nthu.edu.tw

Authors

Po-Ting Lai − *Department of Materials Science and Engineering, National Tsing Hua University, Hsinchu 30013, Taiwan; Frontier Research Center on Fundamental and Applied Sciences of Matters, National Tsing Hua University, Hsinchu 30013, Taiwan;* orcid.org/0000-0002-8464-6364

Cheng-Yueh Chen − *Department of Materials Science and Engineering, National Tsing Hua University, Hsinchu 30013, Taiwan; Frontier Research Center on Fundamental and Applied Sciences of Matters, National Tsing Hua University, Hsinchu 30013, Taiwan*

Hao-Cheng Lin − *Department of Materials Science and Engineering, National Tsing Hua University, Hsinchu 30013, Taiwan; Frontier Research Center on Fundamental and Applied Sciences of Matters, National Tsing Hua University, Hsinchu 30013, Taiwan*

Bo-Yuan Chuang − *Department of Chemistry, National Taiwan University, Taipei 10617, Taiwan*

Kai-Hua Kuo − *Department of Chemistry, National Taiwan University, Taipei 10617, Taiwan*

Christopher R. Greve − *Dynamics and Structure Formation—Herzig Group, University of Bayreuth, 95447 Bayreuth, Germany;* orcid.org/0000-0001-5506-9695

Tsung-Kai Su − *Department of Materials Science and Engineering, National Tsing Hua University, Hsinchu 30013, Taiwan; Frontier Research Center on Fundamental and Applied Sciences of Matters, National Tsing Hua University, Hsinchu 30013, Taiwan*

Guang-Hsun Tan − *Department of Materials Science and Engineering, National Tsing Hua University, Hsinchu 30013, Taiwan; Frontier Research Center on Fundamental and Applied Sciences of Matters, National Tsing Hua University, Hsinchu 30013, Taiwan*

Chia-Feng Li − *Department of Materials Engineering, Ming Chi University of Technology, New Taipei City 24301, Taiwan*

Sheng-Wen Huang − *Department of Materials Engineering, Ming Chi University of Technology, New Taipei City 24301, Taiwan*

Kai-Yuan Hsiao − *Department of Materials Science and Engineering, National Tsing Hua University, Hsinchu 30013, Taiwan*

Eva M. Herzig − *Dynamics and Structure Formation—Herzig Group, University of Bayreuth, 95447 Bayreuth, Germany;* orcid.org/0000-0002-0151-5562

Ming-Yen Lu − *Department of Materials Science and Engineering, National Tsing Hua University, Hsinchu 30013, Taiwan;* orcid.org/0000-0003-1788-1425

Yu-Ching Huang − *Department of Materials Engineering, Ming Chi University of Technology, New Taipei City 24301, Taiwan;* orcid.org/0000-0003-4772-8050

Complete contact information is available at: https://pubs.acs.org/10.1021/acsnano.3c09595

Notes

The authors declare no competing financial interest.

ACKNOWLEDGMENTS

The authors thank the National Science and Technology Council of Taiwan (grant nos. 112-2112-M-007-030-MY3, 112-2636-E-007-002, 111-2634-F-007-007, and 110-2113-M-002-008-MY3) for financial support. The AFM images were performed by scanning probe spectroscopy, the UPS analysis were performed by electron spectroscopy for energy levels analysis, and the TEM images were performed by spherical-aberration-corrected field-emission transmission electron microscope supported by the Instrument Center at NTHU. C.R.G. and E.M.H. are grateful for funding from the Bavarian State Ministry of Science, Research and the Arts through the Collaborative Research Network "Solar Technologies go Hybrid" and made use of DFG (INST 91/443-1).

REFERENCES

(1) Marković, D.; Mizrahi, A.; Querlioz, D.; Grollier, J. Physics for neuromorphic computing. *Nat. Rev. Phys.* **2020**, *2*, 499−510.

(2) van de Burgt, Y.; Melianas, A.; Keene, S. T.; Malliaras, G.; Salleo, A. Organic electronics for neuromorphic computing. *Nat. Electron.* **2018**, *1*, 386−397.

(3) Fuller, E. J.; Keene, S. T.; Melianas, A.; Wang, Z.; Agarwal, S.; Li, Y.; Tuchman, Y.; James, C. D.; Marinella, M. J.; Yang, J. J.; Salleo, A.; Talin, A. A. Parallel programming of an ionic floating-gate memory array for scalable neuromorphic computing. *Science* **2019**, *364*, 570−574.

(4) Burr, G. W.; Shelby, R. M.; Sebastian, A.; Kim, S.; Kim, S.; Sidler, S.; Virwani, K.; Ishii, M.; Narayanan, P.; Fumarola, A.; Sanches, L. L.; Boybat, I.; Le Gallo, M.; Moon, K.; Woo, J.; Hwang, H.; Leblebici, Y. Neuromorphic computing using non-volatile memory. *Adv. Phys.: X* **2017**, *2*, 89−124.

(5) Roy, K.; Jaiswal, A.; Panda, P. Towards spike-based machine intelligence with neuromorphic computing. *Nature* **2019**, *575*, 607−617.

(6) Mao, J.-Y.; Zhou, L.; Zhu, X.; Zhou, Y.; Han, S.-T. Photonic Memristor for Future Computing: A Perspective. *Adv. Opt. Mater.* **2019**, *7*, No. 1900766.

(7) Cheng, Z.; Ríos, C.; Pernice, W. H. P.; Wright, C. D.; Bhaskaran, H. On-chip photonic synapse. *Sci. Adv.* **2017**, *3*, No. e1700160.

(8) Xu, W.; Cho, H.; Kim, Y.-H.; Kim, Y.-T.; Wolf, C.; Park, C.-G.; Lee, T.-W. Organometal Halide Perovskite Artificial Synapses. *Adv. Mater.* **2016**, *28*, 5916−5922.

(9) Huang, C.; Sorger, V. J.; Miscuglio, M.; Al-Qadasi, M.; Mukherjee, A.; Lampe, L.; Nichols, M.; Tait, A. N.; Ferreira de Lima, T.; Marquez, B. A.; Wang, J.; Chrostowski, L.; Fok, M. P.; Brunner, D.; Fan, S.; Shekhar, S.; Prucnal, P. R.; Shastri, B. J. Prospects and applications of photonic neural networks. *Adv. Phys.: X* **2022**, *7*, No. 1981155.

(10) Yang, L.; Singh, M.; Shen, S.-W.; Chih, K.-Y.; Liu, S.-W.; Wu, C.-I.; Chu, C.-W.; Lin, H.-W. Transparent and Flexible Inorganic Perovskite Photonic Artificial Synapses with Dual-Mode Operation. *Adv. Funct. Mater.* **2021**, *31*, No. 2008259.

(11) Xiang, D.; Liu, T.; Xu, J.; Tan, J. Y.; Hu, Z.; Lei, B.; Zheng, Y.; Wu, J.; Neto, A. H. C.; Liu, L.; Chen, W. Two-dimensional multibit optoelectronic memory with broadband spectrum distinction. *Nat. Commun.* **2018**, *9*, 2966.

(12) Park, H.-L.; Kim, H.; Lim, D.; Zhou, H.; Kim, Y.-H.; Lee, Y.; Park, S.; Lee, T.-W. Retina-Inspired Carbon Nitride-Based Photonic Synapses for Selective Detection of UV Light. *Adv. Mater.* **2020**, *32*, No. 1906899.

(13) Mao, J.-Y.; Hu, L.; Zhang, S.-R.; Ren, Y.; Yang, J.-Q.; Zhou, L.; Zeng, Y.-J.; Zhou, Y.; Han, S.-T. Artificial synapses emulated through a light mediated organic−inorganic hybrid transistor. *J. Mater. Chem. C* **2019**, *7*, 48−59.

(14) Dai, S.; Wu, X.; Liu, D.; Chu, Y.; Wang, K.; Yang, B.; Huang, J. Light-Stimulated Synaptic Devices Utilizing Interfacial Effect of Organic Field-Effect Transistors. *ACS Appl. Mater. Interfaces* **2018**, *10*, 21472−21480.

(15) Baeg, K.-J.; Noh, Y.-Y.; Sirringhaus, H.; Kim, D.-Y. Controllable Shifts in Threshold Voltage of Top-Gate Polymer Field-Effect Transistors for Applications in Organic Nano Floating Gate Memory. *Adv. Funct. Mater.* **2010**, *20*, 224−230.

(16) Shih, C.-C.; Chiu, Y.-C.; Lee, W.-Y.; Chen, J.-Y.; Chen, W.-C. Conjugated Polymer Nanoparticles as Nano Floating Gate Electrets for High Performance Nonvolatile Organic Transistor Memory Devices. *Adv. Funct. Mater.* **2015**, *25*, 1511−1519.

(17) Chang, H.-C.; Lu, C.; Liu, C.-L.; Chen, W.-C. Single-Crystal C60 Needle/CuPc Nanoparticle Double Floating-Gate for Low-Voltage Organic Transistors Based Non-Volatile Memory Devices. *Adv. Mater.* **2015**, *27*, 27−33.

(18) Jena, A. K.; Kulkarni, A.; Miyasaka, T. Halide Perovskite Photovoltaics: Background, Status, and Future Prospects. *Chem. Rev.* **2019**, *119*, 3036−3103.

(19) Yamada, Y.; Nakamura, T.; Endo, M.; Wakamiya, A.; Kanemitsu, Y. Photocarrier Recombination Dynamics in Perovskite CH3NH3PbI3 for Solar Cell Applications. *J. Am. Chem. Soc.* **2014**, *136*, 11610−11613.

(20) Quan, L. N.; Rand, B. P.; Friend, R. H.; Mhaisalkar, S. G.; Lee, T.-W.; Sargent, E. H. Perovskites for Next-Generation Optical Sources. *Chem. Rev.* **2019**, *119*, 7444−7477.

(21) Kumar, S.; Jagielski, J.; Yakunin, S.; Rice, P.; Chiu, Y.-C.; Wang, M.; Nedelcu, G.; Kim, Y.; Lin, S.; Santos, E. J. G.; Kovalenko, M. V.; Shih, C.-J. Efficient Blue Electroluminescence Using Quantum-Confined Two-Dimensional Perovskites. *ACS Nano* **2016**, *10*, 9720−9729.

(22) Chen, J.-Y.; Chiu, Y.-C.; Li, Y.-T.; Chueh, C.-C.; Chen, W.-C. Nonvolatile Perovskite-Based Photomemory with a Multilevel Memory Behavior. *Adv. Mater.* **2017**, *29*, No. 1702217.

(23) Li, Q.; Li, T.; Zhang, Y.; Yu, Y.; Chen, Z.; Jin, L.; Li, Y.; Yang, Y.; Zhao, H.; Li, J.; Yao, J. Nonvolatile photoelectric memory with CsPbBr3 quantum dots embedded in poly(methyl methacrylate) as charge trapping layer. *Org. Electron.* **2020**, *77*, No. 105461.

(24) Wang, Y.; Lv, Z.; Chen, J.; Wang, Z.; Zhou, Y.; Zhou, L.; Chen, X.; Han, S.-T. Photonic Synapses Based on Inorganic Perovskite Quantum Dots for Neuromorphic Computing. *Adv. Mater.* **2018**, *30*, No. 1802883.

(25) Gedda, M.; Yengel, E.; Faber, H.; Paulus, F.; Kreß, J. A.; Tang, M.-C.; Zhang, S.; Hacker, C. A.; Kumar, P.; Naphade, D. R.; Vaynzof, Y.; Volonakis, G.; Giustino, F.; Anthopoulos, T. D. Ruddlesden−Popper-Phase Hybrid Halide Perovskite/Small-Molecule Organic Blend Memory Transistors. *Adv. Mater.* **2021**, *33*, No. 2003137.

(26) Chen, Y.; Sun, Y.; Peng, J.; Tang, J.; Zheng, K.; Liang, Z. 2D Ruddlesden−Popper Perovskites for Optoelectronics. *Adv. Mater.* **2018**, *30*, No. 1703487.

(27) Wu, Y.; Xie, F.; Chen, H.; Yang, X.; Su, H.; Cai, M.; Zhou, Z.; Noda, T.; Han, L. Thermally Stable MAPbI3 Perovskite Solar Cells with Efficiency of 19.19% and Area over 1 cm2 achieved by Additive Engineering. *Adv. Mater.* **2017**, *29*, No. 1701073.

(28) Wang, T.; Zhang, H.; Hou, S.; Zhang, Y.; Li, Q.; Zhang, Z.; Gao, H.; Mao, Y. Facile Synthesis of Methylammonium Lead Iodide Perovskite with Controllable Morphologies with Enhanced Luminescence Performance. *Nanomater.* **2019**, *9*, 1660.

(29) Niu, T.; Lu, J.; Jia, X.; Xu, Z.; Tang, M.-C.; Barrit, D.; Yuan, N.; Ding, J.; Zhang, X.; Fan, Y.; Luo, T.; Zhang, Y.; Smilgies, D.-M.; Liu, Z.; Amassian, A.; Jin, S.; Zhao, K.; Liu, S. Interfacial Engineering at the 2D/3D Heterojunction for High-Performance Perovskite Solar Cells. *Nano Lett.* **2019**, *19*, 7181−7190.

(30) Kim, S.-Y.; Yang, J.-M.; Choi, E.-S.; Park, N.-G. Effect of interlayer spacing in layered perovskites on resistive switching memory. *Nanoscale* **2019**, *11*, 14330−14338.

(31) Gao, Y.; Shi, E.; Deng, S.; Shiring, S. B.; Snaider, J. M.; Liang, C.; Yuan, B.; Song, R.; Janke, S. M.; Liebman-Peláez, A.; Yoo, P.; Zeller, M.; Boudouris, B. W.; Liao, P.; Zhu, C.; Blum, V.; Yu, Y.; Savoie, B. M.; Huang, L.; Dou, L. Molecular engineering of organic−inorganic hybrid perovskites quantum wells. *Nat. Chem.* **2019**, *11*, 1151−1157.

(32) Chen, Y.-H.; Lin, L.-Y.; Lu, C.-W.; Lin, F.; Huang, Z.-Y.; Lin, H.-W.; Wang, P.-H.; Liu, Y.-H.; Wong, K.-T.; Wen, J.; Miller, D. J.; Darling, S. B. Vacuum-Deposited Small-Molecule Organic Solar Cells with High Power Conversion Efficiencies by Judicious Molecular Design and Device Optimization. *J. Am. Chem. Soc.* **2012**, *134*, 13616−13623.

(33) Banerjee, W.; Liu, Q.; Lv, H.; Long, S.; Liu, M. Electronic imitation of behavioral and psychological synaptic activities using TiOx/Al2O3-based memristor devices. *Nanoscale* **2017**, *9*, 14442−14450.

(34) Wang, Y.; Liu, E.; Gao, A.; Cao, T.; Long, M.; Pan, C.; Zhang, L.; Zeng, J.; Wang, C.; Hu, W.; Liang, S.-J.; Miao, F. Negative Photoconductance in van der Waals Heterostructure-Based Floating Gate Phototransistor. *ACS Nano* **2018**, *12*, 9513−9520.

(35) Ercan, E.; Lin, Y.-C.; Yang, W.-C.; Chen, W.-C. Self-Assembled Nanostructures of Quantum Dot/Conjugated Polymer Hybrids for

https://doi.org/10.1021/acsnano.3c09595
ACS Nano 2023, 17, 25552−25564

Photonic Synaptic Transistors with Ultralow Energy Consumption and Zero-Gate Bias. *Adv. Funct. Mater.* **2022**, *32*, No. 2107925.
(36) Jin, R.; Wang, J.; Shi, K.; Qiu, B.; Ma, L.; Huang, S.; Li, Z. Multilevel storage and photoinduced-reset memory by an inorganic perovskite quantum-dot/polystyrene floating-gate organic transistor. *RSC Adv.* **2020**, *10*, 43225−43232.
(37) Sun, Y.; Li, M.; Ding, Y.; Wang, H.; Wang, H.; Chen, Z.; Xie, D. Programmable van-der-Waals heterostructure-enabled optoelectronic synaptic floating-gate transistors with ultra-low energy consumption. *InfoMat* **2022**, *4*, No. e12317.
(38) van de Burgt, Y.; Lubberman, E.; Fuller, E. J.; Keene, S. T.; Faria, G. C.; Agarwal, S.; Marinella, M. J.; Alec Talin, A.; Salleo, A. A non-volatile organic electrochemical device as a low-voltage artificial synapse for neuromorphic computing. *Nat. Mater.* **2017**, *16*, 414−418.
(39) Peng, X.; Huang, S.; Luo, Y.; Sun, X.; Yu, S. In DNN +NeuroSim: An End-to-End Benchmarking Framework for Compute-in-Memory Accelerators with Versatile Device Technologies, In *2019 IEEE International Electron Devices Meeting (IEDM)*; IEEE, 2019; pp 32.5.1−32.5.4.
(40) Peng, X.; Huang, S.; Jiang, H.; Lu, A.; Yu, S. DNN+NeuroSim V2.0: An End-to-End Benchmarking Framework for Compute-in-Memory Accelerators for On-Chip Training. *IEEE Trans. Comput.-Aided Des. Integr. Circuits Syst.* **2021**, *40*, 2306−2319.
(41) Seo, S.; Lee, J.-J.; Lee, R.-G.; Kim, T. H.; Park, S.; Jung, S.; Lee, H.-K.; Andreev, M.; Lee, K.-B.; Jung, K.-S.; Oh, S.; Lee, H.-J.; Kim, K. S.; Yeom, G. Y.; Kim, Y.-H.; Park, J.-H. An Optogenetics-Inspired Flexible van der Waals Optoelectronic Synapse and its Application to a Convolutional Neural Network. *Adv. Mater.* **2021**, *33*, No. 2102980.
(42) Lecun, Y.; Bottou, L.; Bengio, Y.; Haffner, P. Gradient-based learning applied to document recognition. *Proc. IEEE* **1998**, *86*, 2278−2324.
(43) Lee, K.; Han, H.; Kim, Y.; Park, J.; Jang, S.; Lee, H.; Lee, S. W.; Kim, H.; Kim, Y.; Kim, T.; Kim, D.; Wang, G.; Park, C. Retina-Inspired Structurally Tunable Synaptic Perovskite Nanocones. *Adv. Funct. Mater.* **2021**, *31*, No. 2105596.
(44) Huang, Y.-C.; Tsao, C.-S.; Cho, Y.-J.; Chen, K.-C.; Chiang, K.-M.; Hsiao, S.-Y.; Chen, C.-W.; Su, C.-J.; Jeng, U. S.; Lin, H.-W. Insight into Evolution, Processing and Performance of Multi-length-scale Structures in Planar Heterojunction Perovskite Solar Cells. *Sci. Rep.* **2015**, *5*, 13657.
(45) Lin, H.-Y.; Chen, C.-Y.; Hsu, B.-W.; Cheng, Y.-L.; Tsai, W.-L.; Huang, Y.-C.; Tsao, C.-S.; Lin, H.-W. Efficient Cesium Lead Halide Perovskite Solar Cells through Alternative Thousand-Layer Rapid Deposition. *Adv. Funct. Mater.* **2019**, *29*, No. 1905163.
(46) Huang, Y.-C.; Li, C.-F.; Huang, Z.-H.; Liu, P.-H.; Tsao, C.-S. Rapid and sheet-to-sheet slot-die coating manufacture of highly efficient perovskite solar cells processed under ambient air. *Sol. Energy* **2019**, *177*, 255−261.
(47) Yang, W.-C.; Chiang, Y.-C.; Lam, J.-Y.; Chuang, T.-H.; Ercan, E.; Chueh, C.-C.; Chen, W.-C. Improving Performance of Nonvolatile Perovskite-Based Photomemory by Size Restrain of Perovskites Nanocrystals in the Hybrid Floating Gate. *Adv. Electron. Mater.* **2020**, *6*, No. 2000458.
(48) Lin, W.; Chen, G.; Li, E.; He, L.; Yu, W.; Peng, G.; Chen, H.; Guo, T. Nonvolatile Multilevel Photomemory Based on Lead-Free Double Perovskite Cs2AgBiBr6 Nanocrystals Wrapped Within SiO2 as a Charge Trapping Layer. *ACS Appl. Mater. Interfaces* **2020**, *12*, 43967−43975.
(49) Li, Q.; Li, T.; Zhang, Y.; Chen, Z.; Li, Y.; Jin, L.; Zhao, H.; Li, J.; Yao, J. Photoerasable Organic Field-Effect Transistor Memory Based on a One-Step Solution-Processed Hybrid Floating Gate Layer. *J. Phys. Chem. C* **2020**, *124*, 23343−23351.
(50) Li, Q.; Li, T.; Zhang, Y.; Zhao, H.; Li, J.; Yao, J. Dual-functional optoelectronic memories based on ternary hybrid floating gate layers. *Nanoscale* **2021**, *13*, 3295−3303.
(51) Lai, H.; Zhou, Y.; Zhou, H.; Zhang, N.; Ding, X.; Liu, P.; Wang, X.; Xie, W. Photoinduced Multi-Bit Nonvolatile Memory Based on a van der Waals Heterostructure with a 2D-Perovskite Floating Gate. *Adv. Mater.* **2022**, *34*, No. 2110278.
(52) Lai, H.; Lu, Z.; Lu, Y.; Yao, X.; Xu, X.; Chen, J.; Zhou, Y.; Liu, P.; Shi, T.; Wang, X.; Xie, W. Fast, Multi-Bit, and Vis-Infrared Broadband Nonvolatile Optoelectronic Memory with MoS2/2D-Perovskite Van der Waals Heterojunction. *Adv. Mater.* **2023**, *35*, No. 2208664.

https://doi.org/10.1021/acsnano.3c09595
ACS Nano 2023, 17, 25552−25564